Vertical TiO₂ Nanorods as a Medium for Stable and High-Efficiency Perovskite Solar Modules

Azhar Fakharuddin,[†,‡] Francesco Di Giacomo,[‡] Alessandro L. Palma,[‡] Fabio Matteocci,[‡] Irfan Ahmed,[†] Stefano Razza,[‡] Alessandra D'Epifanio,[§] Silvia Licoccia,[§] Jamil Ismail,[†] Aldo Di Carlo,[‡] Thomas M. Brown,*[,‡] and Rajan Jose*[,†]

[†]Nanostructured Renewable Energy Materials Laboratory, Faculty of Industrial Sciences and Technology (FIST), Universiti Malaysia Pahang, 26300 Kuantan, Malaysia and [‡]C.H.O.S.E. (Centre for Hybrid and Organic Solar Energy), Department of Electronic Engineering, and [§]Department of Chemical Science and Technologies, University of Rome "Tor Vergata", Rome 00133, Italy

ABSTRACT Perovskite solar cells employing $CH_3NH_3PbI_{3-x}Cl_x$ active layers show power conversion efficiency (PCE) as high as 20% in single cells and 13% in large area modules. However, their operational stability has often been limited due to degradation of the $CH_3NH_3PbI_{3-x}Cl_x$ active layer. Here, we report a perovskite solar module (PSM, best and av. PCE 10.5 and 8.1%), employing solution-grown TiO₂ nanorods (NRs) as the electron transport layer, which showed an increase in performance (∼5%) even after shelf-life investigation for 2500 h.

A crucial issue on the module fabrication was the patterning of the TiO₂ NRs, which was solved by interfacial engineering during the growth process and using an optimized laser pulse for patterning. A shelf-life comparison with PSMs built on TiO₂ nanoparticles (NPs, best and av. PCE 7.9 and 5.5%) of similar thickness and on a compact TiO₂ layer (CL, best and av. PCE 5.8 and 4.9%) shows, in contrast to that observed for NR PSMs, that PCE in NPs and CL PSMs dropped by ∼50 and ∼90%, respectively. This is due to the fact that the $CH_3NH_3PbI_{3-x}Cl_x$ active layer shows superior phase stability when incorporated in devices with TiO₂ NR scaffolds.
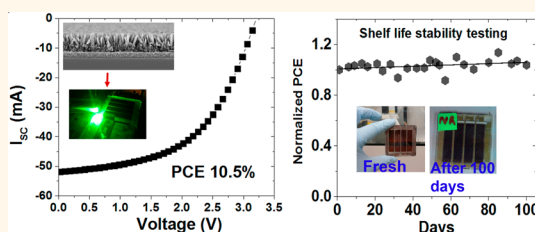
KEYWORDS: nanorod solar cells · energy conversion · stable solar module · photovoltaic

Solution-processed perovskite solar cells (PSCs) have achieved a certified power conversion efficiency (PCE) of 20.1%.[1] Although remarkable progress has been made in laboratory-scale devices,[2−6] there are still only a few reports on large area modules for practical deployment.[7−12] The first solid-state perovskite solar module (PSM) having a PCE of ∼5.1% employing a mesoporous TiO₂ electron transport layer (ETL), a $CH_3NH_3PbI_{3-x}Cl_x$ absorber layer, and a P3HT hole transport medium (HTM) was published in 2014.[8] The PCE was further improved to 13%, the highest in PSM so far, by minimizing the contact resistance (R_{CON}) at the series interconnections *via* precise laser patterning and also using spiro-MeOTAD as HTM.[7] The scalability of these methods was also demonstrated over large area module sizes of ∼100 cm² *via* air-flow-assisted doctor blading and sequential deposition of perovskite precursors at ambient conditions; however, the PCE dropped to ∼4.1%

due to nonuniform HTM deposition during scaling up.[12] Similarly, PSMs employing a planar inverted architecture (ITO/PEDOT: PSS/CH₃NH₃PbI₃/PCBM)[9] and also flexible PSMs[11] on plastic substrates have been reported with a PCE of ∼8.7 and 3.1%, respectively.

While high PCE in PSMs has been achieved together with their fabrication *via* scalable methods such as doctor blading and screen printing, their long-term operational stability remains a bottleneck toward their practical deployment.[13−15] The modules reported have mostly employed either a TiO₂ mesoporous scaffold or a planar architecture.[2−7] The stability in PSCs has been shown to also partially depend on the morphology and crystallinity of the electron transport layers (ETLs).[16] While a planar architecture with a compact TiO₂ layer provided a high initial PCE, it resulted in unstable PSCs compared to those made of a crystalline nanorod (NR) scaffold that
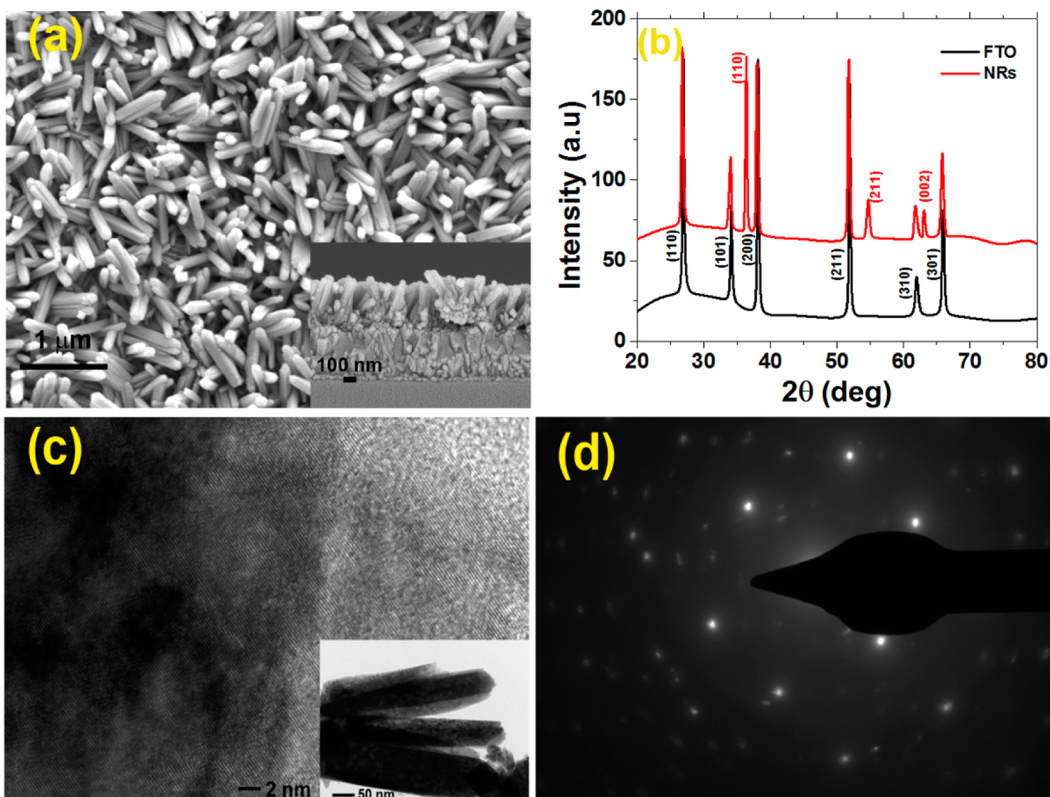
Figure 1. (a) Top view of as-grown rutile nanorods on the FTO surface. Inset shows a cross section of NRs. **(b)** XRD spectra of rutile nanorods compared with a bare FTO. **(c)** Surface monographs of TiO$_2$ NRs using high-resolution transmission electron microscopy. Inset shows a distant view of the same. **(d)** Electron diffraction pattern of annealed rutile NRs. For all measurements, the annealed NRs (450 °C for 30 min) were used.

showed consistent performance with up to 60 days of shelf life.[16] On the other hand, the TiO$_2$ NP-based ETL may induce instability in the PSCs due to light-induced desorption of surface-adsorbed oxygen.[17] The NRs therefore remain a potential scaffold material to build durable devices. Owing to their one-dimensional structure, NRs offer 2 orders of magnitude higher electron mobility, longer diffusion lengths, and improved pore-filling compared to the labyrinthine NP analogues.[18] However, despite the advantages offered by these one-dimensional nanostructures, their research so far has been limited to laboratory-scale devices not only in PSCs but also in their predecessors, the dye solar cells.[19−21] This limitation is due also to the difficulty in patterning them, which is necessary for the up-scaling to module size. In fact, rutile nanorods are routinely synthesized *via* bottom-up processes where they firmly grow on the conducting glass substrate (typically, fluorine-doped tin oxide, FTO).[22] One could argue the possibility of selectively growing these NRs on a prepatterned substrate. However, because the NRs are typically synthesized on conducting substrates *via* a solution approach growing all over the surface, the end-to-end growth leaves no place for cell series interconnection (Figure 1a). Furthermore, NRs grow in a strong acidic medium and at temperatures of ∼150 °C, making it difficult to mask the FTO for NR growth on

selective areas, which could allow patterning of substrates for serial interconnections. The removal of NRs from the interconnection of individual cells is crucial as the presence of NRs adds to the sheet resistance (R_{SHEET}) and contact resistance (R_{CON}), thereby reducing the fill factor (FF). The key challenge for module fabrication, therefore, is to develop a method to pattern the as-grown NRs *via* their selective removal.

Herein, we demonstrate successful removal of the NRs from selective areas of FTO *via* interfacial engineering during a growth process and controlled laser pulsing for developing monolithic series type CH$_3$NH$_3$PbI$_{3−x}$Cl$_x$ modules. The NRs grown directly on FTOs could not be patterned even at high laser powers; this issue was solved by growing them on an intermediate thin TiO$_2$ layer on FTO. The NRs were ablated from the FTO without damaging the conducting layer, resulting in R_{SHEET} and R_{CON} (∼25 Ω/□ and ∼4 Ω/mm^2, respectively), closer to that of a bare FTO (R_{SHEET} ∼ 15 Ω/□, R_{CON} 1.6 Ω/mm^2). The precisely laser-patterned substrates with the TiO$_2$ NRs, when employed to fabricate PSMs, resulted in a PCE of ∼10.5%, significantly higher than that of reference modules made either with TiO$_2$ NPs (7.9%) or with just a compact TiO$_2$ layer in the planar architecture (5.8%). The encapsulated NR PSMs also showed a remarkably stable performance over the ∼2500 h of our study compared to PSMs employing
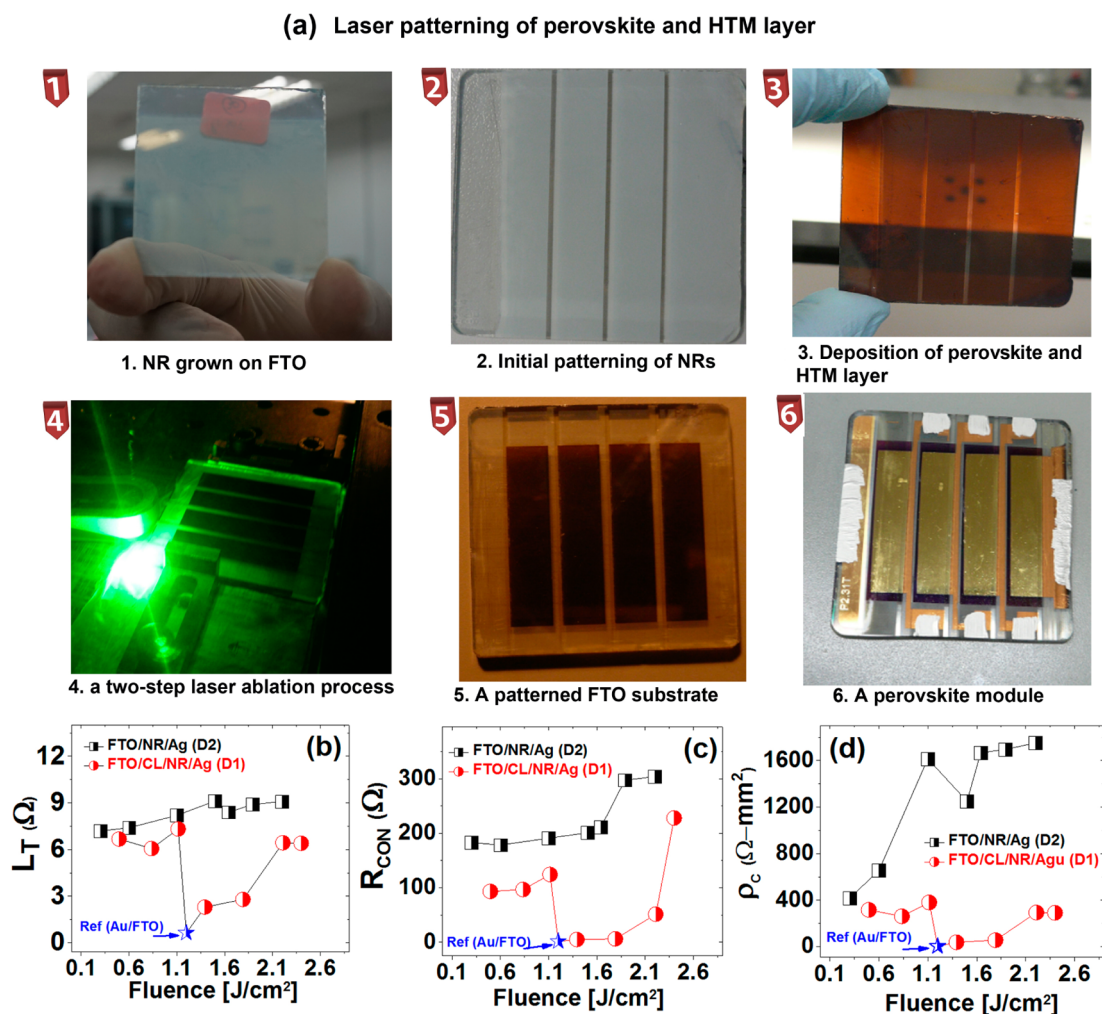
(a) Laser patterning of perovskite and HTM layer

1. NR grown on FTO

2. Initial patterning of NRs

3. Deposition of perovskite and HTM layer

4. a two-step laser ablation process

5. A patterned FTO substrate

6. A perovskite module

Figure 2. (a) Step-by-step fabrication of perovskite modules made of TiO_2 nanorods. (b–d) Specific contact resistivity (ρ_C), contact resistance (R_{CON}), and transfer length (L_T) calculated *via* the transfer length method of the FTO substrates used for fabricating the two device architectures, D1 (FTO/NR, represented by circles in the graph) and D2 (FTO/IL/NR, represented by squares symbols in figure).

RESULTS AND DISCUSSION

Patterning of Solution-Grown TiO₂ Nanorods. Morphology and crystal structure of the as-grown TiO_2 NRs are shown in Figure 1. The NRs have an average diameter of ~100 nm, a length of ~500−550 nm, and a packing density ~3.8×10^{10} cm^{-2} (Figure 1a). All of the peaks in the X-ray diffraction (XRD) pattern shown in Figure 1b could be indexed to rutile TiO_2 in addition to the ones from the fluorine-doped tin oxide substrate. Lattice parameters of the TiO_2 nanorods determined from the XRD patterns are $a = b = 4.59$ Å and $c = 2.95$ Å, which are in good agreement with the reported values (ICDD 00-001-1292). The rods were single crystalline, as judged from the extended crystallinity of the lattice images (Figure 1c) and spotty electron diffraction pattern (Figure 1d).

The NRs were grown all over the FTO surface during the hydrothermal process, thereby leaving no space between individual cells for series interconnections (Figure 1a). To make individual cell contacts and interconnections between them, the NRs were selectively removed using an Nd:YVO₄ laser pulsed (~18 ns) at ~10 kHz at an optimized output laser fluence of 1.4−2.0 J cm^{-2}. A thin intermediate layer (IL) of ~50 nm thick TiO_2 was deposited *via* a $TiCl_4$ solution treatment on FTO (NR/IL/FTO, D2) before the growth of the NR. Details of the optimization procedures of laser power and the effect of laser treatment on both types of device architectures, D1, with the NR grown directly on FTO, and D2, incorporating the IL before the NR growth, are provided in Supporting Information (Figures SI-3, SI-4, SI-6, and SI-7). Figure 2b−d shows the contact resistivity (ρ_C), R_{CON}, and the transfer length (L_T) *via* transfer length method (TLM) of both device architectures (D1 and D2) as a function of laser fluence. The fact that, at laser fluences between 1.4 and 1.8 J cm^{-2},

TiO₂ NPs and nanoporous compact layers in similar experimental conditions, affirming the crucial role of the nature of the ETLs and scaffolds on module stability.
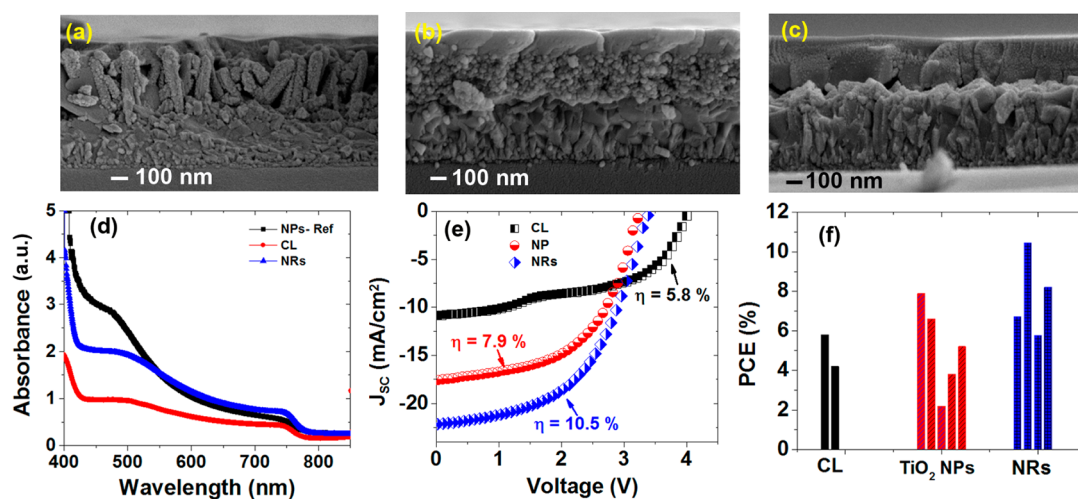
Figure 3. (a−c) Cross-sectional view of the three devices, with different NR, NP, and CL electron collecting layers, respectively. (d) Absorbance spectra of the three devices immediately after fabrication. (e) Current−voltage characteristics of the three ETL modules recorded at AM1.5G and at 100 W/cm^2. (f) Graph showing the PCE of a different number of modules (2 for CL, 5 for NP, and 4 for NR electron collecting layers) fabricated in our experiments.

TABLE 1. Photovoltaic Parameters (J_{SC}, V_{OC}, FF, and PCE) of the CL, NP, and NR Modules and the Average PCE with Standard Deviation Calculated over All Fabricated Modules

device architecture	area (cm^2)	I_{SC} (mA)	J_{SC} (mA/cm^2)	V_{OC} (V)	FF	best PCE (%)	av. PCE (%)
CL	10.8 (2.7 cm^2 × 4)	29.2	10.8	4.06	0.53	5.8	4.9 ± 1.1
NP	10.8 (2.7 cm^2 × 4)	47.8	17.7	3.24	0.55	7.9	5.5 ± 2.1
NR	10.8 (2.7 cm^2 × 4)	57.1	22.2	3.37	0.56	10.5	7.8 ± 2.0

these parameters are close to those of a bare FTO sample represents evidence that there has been a successful removal of NR from D2, which makes it favorable for building large area modules (Figure SI-4). The IL played a crucial role in the successful ablation of the NRs; in the device architecture D1, the NRs could not be removed from the FTO surface at laser fluences that would not damage the FTO (<2 J cm^{-2}). This is because the adhesion of NRs on the FTO surface is stronger compared to that of NRs grown on the IL. The FTO surface was damaged at higher laser powers (Figure SI-5), eventually resulting in a several-fold increase of R_{CON}.

The microstructure at the interface and thickness of the functional layers of the devices, studied by scanning electron microscopy (SEM), show that the thicknesses of TiO_2−$CH_3NH_3PbI_{3−x}Cl_x$ in NRs, NPs, and CL devices were ∼460, ∼510, and ∼100 nm, respectively (Figure 3a−c). No perovskite overlayer is visible in the devices, as the perovskite infiltrated through the pores of ETLs. The $CH_3NH_3PbI_{3−x}Cl_x$ crystallized on NRs and CL as nanoparticles (with characteristic sizes of 10−30 nm, Figure SI-8), whereas its formation on TiO_2 NPs was not clearly visible, conceivably due to the conformal coating of the perovskite layer on the TiO_2 NP.[5,14]

ETL-Dependent Photovoltaic Performance. Current−voltage characteristics of the devices, measured at 1 sun

conditions (Figure 3e), demonstrated that the photovoltaic (PV) performance of PSCs is strongly influenced by the ETL. The PCE (calculated for forward scan (scan rate 40 mV/s) with respect to active area = $I_{SC} \times V_{OC} \times$ FF/active area) for the best performing CL and TiO_2 NPs were ∼5.8 and ∼7.9%, respectively, calculated on the active area. Detailed IV parameters and average PCE of the modules are given in Table 1. X-ray diffraction and absorbance measurements of the devices show that the NR PSMs have a larger volume fraction of the perovskite, which explains the origin of higher J_{SC} and PCE in them. The best performing NR-based module resulted in significantly higher PV parameters, that is, $V_{OC} \sim 3.36$ V, $J_{SC} \sim 22.2$ mA/cm^2, FF ∼ 0.56, and PCE ∼ 10.5% with respect to active area. To ensure consistency and reliability of our experimental results, data from all of the fabricated devices are shown in Figure 3f. The PCE values for two CL, five NP, and four NR modules fabricated at similar experimental conditions and in different batches were 5 ± 1.1, 5.4 ± 2.1, and 7.8 ± 2%, respectively. Higher J_{SC} values were routinely observed in NR modules (19.2 ± 2.78 mA/cm^2), evidencing the beneficial effects when 1D materials are employed as the ETL.

The nonuniform deposition of the perovskite layer and HTM over ETL induced internal hysteresis in NP and NR devices, resulting in V_{OC} comparatively lower than that in a planar module.[23−25] A similar trend
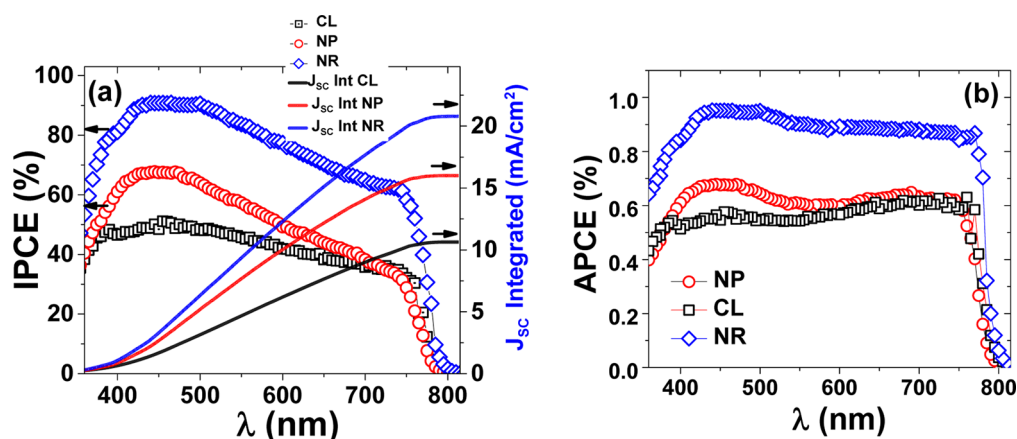
Figure 4. (a) IPCE spectra of the three devices and their integrated photocurrent calculated from the overlap of the IPCE spectrum with AM1.5G solar photon flux and (b) APCE spectra of the three ETM modules calculated from their IPCE and LHE. In (a), the IPCE of CL, NP, and NR is represented by □, ○, and ◊, whereas the colored lines represent integrated photocurrent of the same devices, respectively.

correlation between hysteresis and V_{OC} is observed by Kim et al.,[25] where V_{OC} showed a strong dependence on the calculated hysteresis index. We note that the photovoltaic parameters in the NP-based PSMs are slightly higher than those in our previous report (V_{OC} = 3.36 V, I_{SC} = 35.7 mA, J_{SC} = 14.2 mA/cm^2, FF = 0.65, and PCE = 7.7%),[7] which employed a NP ETL thickness of ~250 nm (see Figure 5 of ref 7). The increased performance in the present work can be attributed to higher perovskite loading, due to the higher TiO$_2$ layer thickness (~500 nm). On the other hand, the significantly higher PV performance in NR modules is due to improved charge collection compared to their NP analogue of similar thickness (~500 nm), as explained subsequently in this article. The significantly higher photocurrent in NRs can be attributed to two reasons. First, their one-dimensional morphology reduced transport resistance in the NR and charge recombination at the NR/CH$_3$NH$_3$PbI$_{3-x}$Cl$_x$ interface compared to the NP counterparts, as evident from their increased FF and V_{OC}. Second, significantly higher absorbance and light scattering in NR modules below 600 nm can be noted (Figure 3d), which is attributed to the bigger size of NRs (~100 nm diameter and ~500 nm length) compared to the size of the NPs (~25 nm). Although the planar module with the CL resulted in significantly higher V_{OC}, commonly observed in these devices as explained in a previous report,[16] the final PCE is limited due to inferior J_{SC}. The lower photocurrent in CL devices compared to the NP and NR modules can be mainly ascribed to their significantly lower absorbance (Figure 3d) and partially to the absence of additional light scattering from the ETL.

Incident photon-to-current conversion efficiency (IPCE) investigations validated the improved PV parameters of NR modules. Figure 4a shows the IPCE spectra of the three modules. The photocurrent generation starts in the near-IR (~800 nm), which is in agreement with the band gap of perovskite[26] and

reaches its maximum value of ~90% near ~450 nm, at the short wavelength end of the spectrum. The integrated J_{SC} values for CL, NP, and NR modules, calculated by integrating IPCE spectra with the photon flux at 1 sun conditions, are 10.4, 16.4, and 21.3 mA/cm^2, respectively, which are in good agreement with the measured J_{SC} (10.2, 17.6, and 22.2 mA/cm^2, respectively). The IPCE values gradually decreased above ~500 nm, which is due to the lower light harvesting efficiency (LHE, i.e., percentage of incident light absorbed) of CH$_3$NH$_3$PbI$_{3-x}$Cl$_x$ in this region (Figure SI-9a). The improved PV performance and charge collection in NR modules is also reflected from their absorbed photonto-current conversion efficiency (APCE, internal quantum efficiency) spectrum (Figure 4b), which is defined as the ratio between the number of photoelectrons collected in a solar cell and the number of photons absorbed. The APCE (IPCE/LHE) spectrum shows near unity quantum yield in NR modules for generated and collected charge carriers throughout the visible region of solar spectrum, significantly higher than NP and CL devices (~70 and ~60%, respectively). A comparison of APCE values of the three devices with their J_{SC} shows that the improved performance in NR modules is not only due to their higher absorbance compared to NP and CL devices but also, more importantly, from their improved charge collection at similar thickness owing to their one-dimensional nature.

Effect of ETL on the Durability of PSMs. In order to evaluate the effect of the ETLs on the long-term performance of perovskite solar modules, we carried out shelf-life investigations (ISOS-D-1 Shelf)[27] for ~2500 h of a batch of encapsulated modules consisting of three NR, three NP, and one CL module. All of the devices showed similar performance over 2500 h of shelf-life investigation. CL (planar) devices have been known to degrade in a similar fashion;[16] therefore, only one module was tested for aging. The three types of modules showed a rapid decrease in PV performance
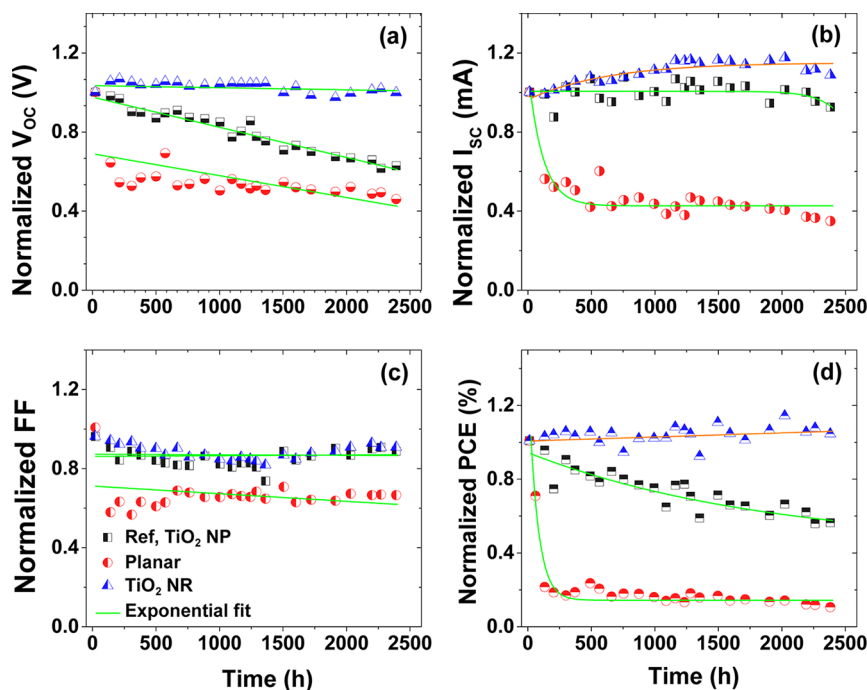
Figure 5. (a—d) Normalized V_{OC}, J_{SC}, FF, and PCE of the three encapsulated modules (NR, NP, and CL represented by a triangle, square, and circle symbol, respectively) measured during a shelf-life investigation for ~2500 h.

after encapsulation at ~110 °C (Figure SI-11) due to thermal shock during the encapsulation procedure. However, the performance mostly recovered within ~100 h, so that the stress caused by thermal shock is to a certain extent reversible. The aging trends of the three modules show a rapid decay in the performance of CL devices within the first 500 h (Figure 5); the PCE dropped by 80% (following the same trend as that of its J_{SC}), whereas the NP modules showed a gradual decrease in performance over time and a 50% drop in PCE was observed after ~2500 h. The NR module, however, showed a minor increase in performance (4%) during ~2500 h as a result of a slight improvement in its J_{SC}. The shelf life (τ_{EL}) of the three devices calculated from their PCE curves (Figure SI-12 and Table SI-1) shows that τ_E values for NP and CL modules were 2.5 years and 27 days, while the performance of the NR modules did not decrease but actually increased over the shelf-life time of 2500 h. Unlike the thermal shock, degradation of the perovskite phase in encapsulated PSMs over time during the shelf-life tests was irreversible, the reason for which we investigated using absorption and XRD spectroscopy studies.

Degradation in PSCs has mainly been attributed to the decomposition of perovskite crystals into PbI_2.[28−31] The decomposition could be visibly identified from a color change in these devices. Habisreutinger et al.[32] highlighted the crucial role of humidity in the decomposition of $CH_3NH_3PbI_3$, as judged from the color change as well as the decrease of absorbance in their unencapsulated devices. The encapsulated devices in our study did not show any color change after ~2500 h

(Figures SI-13 and SI-14); therefore, the observed reduction of the PV performance in NP and CL PSMs does not likely originate from humidity-induced degradation.

To identify the source of the varied photovoltaic performance of the three modules, we recorded the XRD (Figure 6a—c) patterns of analogues unencapsulated perovskite solar cells kept at low humidity conditions (≤30%) during various stages of aging. The analogues are made due to the difficulty in recording the XRD spectra of the encapsulated larger modules. All three types of devices initially showed XRD peaks of the perovskite phase (14.13, 28.4, and 43.4° corresponding to (110), (220), and (330) planes, respectively), FTO, and TiO_2 only. Upon aging, the devices based on CL and NP showed the nucleation and growth of PbI_2 [$2\theta \sim 12.2°$, (001) plane] at aging time of <600 h, thereby showing the degradation of the $CH_3NH_3PbI_{3−x}Cl_x$ crystal. In addition, the peaks of the perovskite phase continuously shifted to higher angles. On the other hand, the smaller PbI_2 peak in NR-based devices observed at ~1000 h demonstrates lesser and slower degradation of $CH_3NH_3PbI_{3−x}Cl_x$. These observations indicate that the $CH_3NH_3PbI_{3−x}Cl_x$ perovskite in planar and NP-based devices would decompose in the presence of moisture (unencapsulated cells kept at <35% relative humidity), which could be due to the interface morphology also. Upon aging, the $CH_3NH_3PbI_{3−x}Cl_x$ decomposes into PbI_2, and its peak systematically increased, evidencing an increased in PbI_2 in the absorber layer. Although NR-based devices marked the presence of PbI_2 at ~1000 h, its growth rate is appreciably lower than that of the other devices.
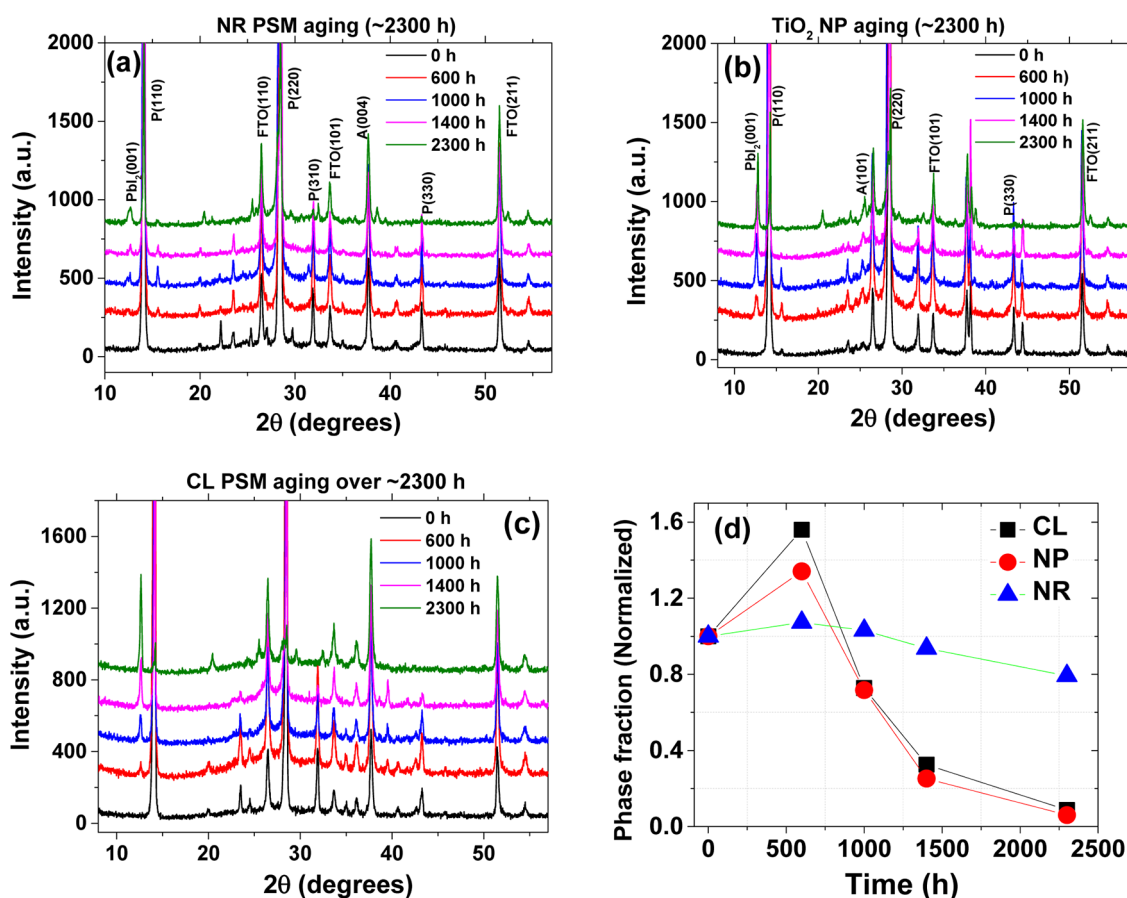
Figure 6. (a—c) XRD spectra of the three devices with different ETLs (unencapsulated, employing TiO_2, perovskite and HTM layers only) measured for ~2300 h, stored in low humidity conditions and in the dark, and (d) fraction of decomposed perovskite crystals calculated from the strongest XRD peaks of the perovskite (14.13 and 28.4°). The labels in the XRD peak indexing A, R, FTO, P, and PbI_2 correspond to anatase, rutile, FTO, perovskite, and PbI_2, respectively.

To identify the lower degradation rate in NR devices, the fraction of the perovskite phase left in the absorber layer of the devices was determined from the area of its main peaks at (110) and (220) planes (14.13 and 28.4°) and is shown in Figure 6d (Figure SI-15). The perovskite degradation rate determined in this way followed an exponential trend, similar to that observed for the PV efficiency and J_{SC}, in which the CL- and NP-based devices were left with <5% perovskite phase against ~80% for NR counterparts after ~2300 h. However, we observed an increasing volume fraction of the perovskite phase at ~600 h together with PbI_2 in CL and NP devices, which could originate from crystallization of the amorphous fraction left during deposition. Given the similar chemical nature of the interface, viz., TiO_2–$CH_3NH_3PbI_{3-x}Cl_x$, the observed perovskite stability in the NR PSMs could originate from two possible reasons: (i) rutile (NR) is thermodynamically more stable than the anatase (CL and NP) so that the TiO_2–$CH_3NH_3PbI_{3-x}Cl_x$ interface is chemically stable; and (ii) nanorods are in thermodynamic equilibrium due to their single crystallinity and larger volume (~4.7 × 10⁶ nm³), whereas polycrystallinity and smaller volume (~8.2 × 10³ nm³) of the CL and NP layers make

them relatively unstable. The second possibility allows migration of ions across the TiO_2–$CH_3NH_3PbI_{3-x}Cl_x$ interface in CL and NP films, thereby degrading the perovskite phase over a period of time. To validate these possibilities, we have developed an overlayer of anatase TiO_2 particles on the NRs by $TiCl_4$ treatment, and the resulting structure was used for PSM fabrication. The PSM thus developed showed a decay behavior similar to that of the NP PSM (Figure SI-17), thereby affirming the beneficial effect of the crystalline NR ETL toward their stable performance.

As unencapsulated NR devices have shown significantly lesser degradation at low humidity conditions, their encapsulated counterparts should show a stable perovskiste phase. To validate the stability of the encapsulated devices, we recorded their absorption and IPCE spectra of the aged devices. The absorbance of CL and NP PSMs decreased significantly in the 650—800 nm wavelength window of the spectrum (Figure 7a), implying significant degradation of the perovskite phase upon aging. On the other hand, NR PSMs showed a slightly increased absorbance in the corresponding region, demonstrating stable perovskite phase and subsequent improvement in the PV
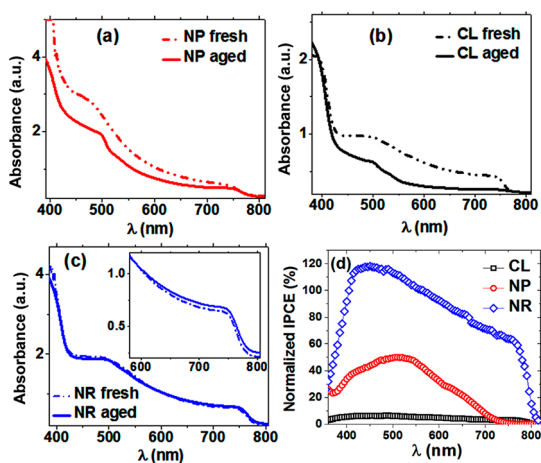
Figure 7. (a−c) Absorbance and IPCE spectra of the three types of the encapsulated modules, used for aging tests, recorded after ∼2500 h. In the absorbance spectra, the dashed line represents absorbance of the fresh device, and the solid line shows absorbance after 2500 h. (d) IPCE spectra of each module are normalized with respect to the IPCE peak value of each device under aging measured immediately after fabrication.

parameters (Figure 7c; inset shows a slight increase in absorbance between 600 and 800 nm). The significantly higher degradation in NP and CL devices can also be confirmed from their IPCE spectra recorded after ∼2500 h; while the IPCE of NP and CL PSMs

dropped by ∼55 and ∼85% compared to their initial values with respect to their peak IPCE values, the NR modules showed an ∼18% increase to their initial IPCE value. Although complete investigations on why NRs led to a durable performance are required, our initial findings serve as a step forward for the commercial deployment of this emerging class of solar cells.

CONCLUSION

We have fabricated $CH_3NH_3PbI_{3−x}Cl_x$-based solar modules employing vertically aligned TiO_2 nanorods as an electron transport layer *via* precise laser patterning and interfacial engineering. Fabrication of an intermediate thin TiO_2 layer between FTO and NRs facilitated their patterning for module fabrication without damaging the conducting oxide layer. The NR modules showed not only significantly higher power conversion efficiency (10.5%, av. 8.1%) compared to the planar (CL, 5.8%, av. 4.9%) architecture and even nanoparticle (NP, 7.9%, av. 5.4%) analogue with the same scaffold thickness but also, more importantly, a higher shelf-life durability. The source of stable performance in NR modules investigated *via* XRD, absorption, and IPCE studies shows that perovskite has a phase stability on NRs better than that of their particle analogues, most likely due to their macroporous nature compared to mesoscopic NPs.

METHODS

Synthesis of Electron Transport Layers on Large Area Substrates. Three types of ETLs were synthesized on large area precleaned conducting glass substrates, FTO (5.7 cm × 5.7 cm^2 purchased from Solaronix, sheet resistance ∼15 Ω/□): (i) ETL employing TiO_2 nanorods, (ii) compact TiO_2 layer *via* $TiCl_4$ solution treatment (CL), and (iii) ETL employing TiO_2 nanoparticle as a scaffold (NPs). Rutile nanorods were prepared as reported elsewhere.[33] In brief, DI water and HCl (37%) were mixed (60 mL/60 mL) and magnetically stirred for 10 min followed by addition of 2.4 mL of titanium isopropoxide until a clear solution was obtained. FTOs were placed in an autoclave containing a Teflon socket with conducting side facing down at an angle ∼45° and kept at 150 °C for 4−5 h in an electric oven to achieve a desired thickness of TiO_2 NRs. Two types of photoanode architectures were obtained for NRs: (i) NRs were directly grown on FTO (single-layer architecture) and labeled D1 (FTO/NR); and (ii) an intermediate layer was grown on the FTO *via* $TiCl_4$ treatment as described in literature,[34] which was then placed in an autoclave for NR growth (double layer) and was labeled D2 (FTO/IL/NR).

To fabricate devices employing TiO_2 NPs, a compact layer was deposited by spray pyrolysis technique on the glass−FTO substrates. A TiO_2 NP paste was then deposited by screen printing and sintered to obtain a ∼500 nm thick mesoporous TiO_2 layer. Thickness of the ETLs was measured using a surface profilometer (Dektak Veeco 150).

Laser Ablation of Electron Transporting Layers. The NRs and CL layers were deposited *via* a bottom-up approach, and the grown ETLs cover the entire FTO surface, unlike the TiO_2 NPs, where a pattened ETL was obained *via* screen printing (Figure SI-20). The insulation of successive cells is, therefore, crucial to realize the series connections that imply electrical contacts between the FTO of the cell to the counter electrode of the adjacent one. To realize such a patterning, we used a Nd:YVO₄ raster scanning

laser emitting at λ = 1064 nm. First, we insulated sequential cells by ablating both FTO and ETL with a repetition rate of 30 kHz at an applied fluence of 4.5 J cm^{-2}, and then we removed the ETL from the area where the FTO makes contact with the counter electrode of the successive cell. The laser parameters were optimized to remove NRs from the FTO surface.

Transfer Length Method Measurements. TLM was employed to investigate ohmic contacts and to measure the contact resistance between different layers on the NR substrates. Although removal of NRs can be visibly confirmed from the substrate (Figures SI-4 and SI-6), TLM measurements are crucial to provide details of sheet resistance (R_{SHEET}) and contact resistance (R_{CON}) of the substrate. We investigated Ag/NR/FTO and Au/NR/IL/FTO after laser ablation, as shown in Figure 2b−d. A Au/FTO contact was used as reference. FTO was scribed *via* laser etching and metal contacts (Ag) were screen printed on the FTO to obtain the desired TLM layout (Figure SI-6), with the distance of the contacts varying from ∼1 to ∼6 mm.

Perovskite and HTM Deposition. We employed single-step perovskite deposition throughout the experiment as reported previously.[8] In brief, methylammonium iodide (Dyesol) and $PbCl_2$ (Aldrich, 98%) were used as received. Mixed perovskite precursor solution ($CH_3NH_3PbI_{3−x}Cl_x$, 40 wt %) was deposited by spin-coating at the three types of ETL (spinning parameters: 2000 rpm for 50 s) inside a glovebox. The $CH_3NH_3PbI_{3−x}Cl_x$ deposited substrates were sintered as follows: 100 °C for 1 h, 110 °C for 15 min, and 120 °C for 15 min. The color change of the samples was observed during the annealing process, showing the crystallization of $CH_3NH_3PbI_{3−x}Cl_x$. The devices were subsequently spin-coated with a hole-conducting medium, 2,20,7,70-tetrakis(*N*,*N*-dip-methoxyphenylamine)9,90-spirobifluorene (Spiro-O-MeTAD 99%, Lumtec, Taiwan), in a solution at 2000 rpm for 50 s in the glovebox and then left in air for 4 h in a closed drybox. The HTM solution was prepared by adding 75 mg of Spiro-O-MeTAD (Lumtec) in 1 mL of chlorobenzene, followed

by addition of 8 μL of 4-*tert*-butylpyridine and 14.2 μL of a 520 mg mL^{-1} LiN(CF$_3$SO$_2$)$_2$N solution in acetonitrile. For metal back contact (Au, ~100 nm), the devices were introduced into a high-vacuum chamber (10^{-6} mbar) for thermal evaporation. The evaporation masks defined the active area of modules (typically 10.8 cm^2 for each module). Four modules of NRs, two modules for planar, and five modules employing TiO$_2$ NP ETL were fabricated and tested to ensure reliability of the experimental results.

Perovskite and HTM Removal Procedure. Perovskite and HTM layers deposited *via* spin-coating on FTO were etched from the interconnections between successive cells using a raster scanning Nd:YVO$_4$ laser, emitting at λ = 532 nm with a pulse duration of ~18 ns and a fluence of 15 mJ/cm^2. We ablated TiO$_2$ NRs, perovskite, and HTM over the patterned FTO using one-step ablation (Figure 2a); first, the λ = 532 nm raster scanning laser was used to remove the perovskite−HTM layers, and then the 1064 nm raster scanning laser was used to remove NRs from substrates using the same parameters described above.

Electrical Characterization of the Modules. Scanning electron microscopy (7800F, FESEM, JEOL, USA) was used to investigate the morphology of the perovskite grown on the three ETLs *via* cross-sectional analysis of thin films on FTO. Absorption and transmittance of the devices were recorded using a UV−vis spectrophotometer (Shamidzu, UV-2600) employing an integrated sphere. Current−voltage curves of the devices were measured using a class A solar simulator (ABET Sun 2000) at 1 sun illumination conditions using a Keithley 2420 as a source meter and calibrated using a reference silicon cell (RERA Solutions RR-1002). The first measurement of all the devices was made immediately after fabrication.

Device Encapsulation and Long-Term Shelf-Life Investigations. The modules were sealed after first I−V measurement using a 2 mm thick glass using Surlyn (60 μm) as a thermoplastic sealant to investigate the effect of various ETLs on their long-term performance. The lamination was performed with a Memo pneumatic flat hot press set at 110 °C. The encapsulated devices were kept in air in a closed box containing silica desiccant (relative humidity <35%) following the protocols (ISOS-D-1 Shelf) reported for the shelf-life investigation.[26] The encapsulated modules are conceivably humidity free over long-term aging, keeping them in low humidity conditions will ensure no or minimum water ingress in these devices.

Conflict of Interest: The authors declare no competing financial interest.

Supporting Information Available: The Supporting Information is available free of charge on the ACS Publications website at DOI: 10.1021/acsnano.5b03265.

Morphology of nanorods, details of laser ablation process and interfacial engineering, transfer length measurements, perovskite deposition on various ETLs, optical and IPCE investigation of modules, thermal degradation of modules, calculation of device lifetime, photographs of modules under stability investigations, XRD investigation and calculation of perovskite phase, and photographs of modules-fabrication (PDF)

REFERENCES AND NOTES

1. National Renewable Energy Laboratory; Best Cell Efficiency Report, 2014; http://www.nrel.gov/ncpv/images/efficiency_chart.jpg (accessed April 2015).

2. Zhou, H.; Chen, Q.; Li, G.; Luo, S.; Song, T. B.; Duan, H. S.; Hong, Z.; You, J.; Liu, Y.; Yang, Y. Interface Engineering of Highly Efficient Perovskite Solar Cells. *Science* **2014**, *345*, 542–546.

3. Im, J. H.; Jang, I.-H.; Pellet, N.; Grätzel, M.; Park, N. G. Growth of CH$_3$NH$_3$PbI$_3$ Cuboids with Controlled Size for High-Efficiency Perovskite Solar Cells. *Nat. Nanotechnol.* **2014**, *9*, 927.

4. Xing, G.; Mathews, N.; Sun, S.; Lim, S. S.; Lam, Y. M.; Gratzel, M.; Mhaisalkar, S.; Sum, T. C. Long-Range Balanced Electron-And Hole-Transport Lengths in Organic-Inorganic CH$_3$NH$_3$PbI$_3$. *Science* **2013**, *342*, 344–347.

5. Burschka, J.; Pellet, N.; Moon, S. J.; Humphry-Baker, R.; Gao, P.; Nazeeruddin, M. K.; Grätzel, M. Sequential Deposition as a Route to High-Performance Perovskite-Sensitized Solar Cells. *Nature* **2013**, *499*, 316–319.

6. Lee, M. M.; Teuscher, J.; Miyasaka, T.; Murakami, T. N.; Snaith, H. J. Efficient Hybrid Solar Cells Based on Meso-Superstructured Organometal Halide Perovskites. *Science* **2012**, *338*, 643–647.

7. Matteocci, F.; Cinà, L.; Di Giacomo, F.; Razza, S.; Palma, A. L.; Guidobaldi, A.; D'Epifanio, A.; Licoccia, S.; Brown, T. M.; Reale, A.; et al. High Efficiency Photovoltaic Module based on Mesoscopic Organometal Halide Perovskite. *Prog. Photovoltaics* **2014**, 10.1002/pip.2557.

8. Matteocci, F.; Razza, S.; Di Giacomo, F.; Casaluci, S.; Mincuzzi, G.; Brown, T. M.; D'Epifanio, A.; Licoccia, S.; Di Carlo, A. Solid-State Solar Modules Based on Mesoscopic Organometal Halide Perovskite: A Route Towards the Up-Scaling Process. *Phys. Chem. Chem. Phys.* **2014**, *16*, 3918–3923.

9. Seo, J.; Park, S.; Kim, Y. C.; Jeon, N. J.; Noh, J. H.; Yoon, S. C.; Seok, S. I. Benefits of Very Thin PCBM and Lif Layers for Solution-Processed P-i-N Perovskite Solar Cells. *Energy Environ. Sci.* **2014**, *7*, 2642–2646.

10. Sfyri, G.; Kumar, C. V.; Raptis, D.; Dracopoulos, V.; Lianos, P. Study of Perovskite Solar Cells Synthesized under Ambient Conditions and of the Performance of Small Cell Modules. *Sol. Energy Mater. Sol. Cells* **2015**, *134*, 60–63.

11. Giacomo, F. Di; Zardetto, V.; D'Epifanio, A.; Pescetelli, S.; Matteocci, F.; Razza, S.; Di Carlo, A.; Licoccia, S.; Kessels, W. M. M.; Creatore, M.; et al. Flexible Perovskite Photovoltaic Modules and Solar Cells Based on Atomic Layer Deposited Compact Layers and UV-Irradiated TiO$_2$ Scaffolds on Plastic Substrates. *Adv. Energy Mater.* **2015**, 10.1002/aenm.201401808.

12. Razza, S.; Di Giacomo, F.; Matteocci, F.; Cinà, L.; Palma, A. L.; Casaluci, S.; Cameron, P.; D'Epifanio, A.; Licoccia, S.; Reale, A.; et al. Perovskite Solar Cells and Large Area Modules (100 cm^2) Based on an Air Flow-Assisted PbI$_2$ Blade Coating Deposition Process. *J. Power Sources* **2015**, *277*, 286–291.

13. Green, M. A.; Ho-Baillie, A.; Snaith, H. J. The Emergence of Perovskite Solar Cells. *Nat. Photonics* **2014**, *8*, 506–514.

14. Grätzel, M. The Light and Shade of Perovskite Solar Cells. *Nat. Mater.* **2014**, *13*, 838–842.

15. Niu, G.; Guo, X.; Wang, L. Review of Recent Progress in Chemical Stability of Perovskite Solar Cells. *J. Mater. Chem. A* **2015**, *3*, 8970–8980.

16. Fakharuddin, A.; Di Giacomo, F.; Ahmed, I.; Wali, Q.; Brown, T. M.; Rajan, J. Role of Morphology and Crystallinity of Nanorod and Planar Electron Transport Layers on the Performance and Long Term Durability of Perovskite Solar Cells. *J. Power Sources* **2015**, *283*, 61–67.

17. Leijtens, T.; Eperon, G. E.; Pathak, S.; Abate, A.; Lee, M. M.; Snaith, H. J. Overcoming Ultraviolet Light Instability of Sensitized TiO$_2$ with Meso-Superstructured Organometal Tri-Halide Perovskite Solar Cells. *Nat. Commun.* **2013**, *4*, 2885.

18. Kim, H. S.; Lee, J. W.; Yantara, N.; Boix, P. P.; Kulkarni, S. A.; Mhaisalkar, S.; Grätzel, M.; Park, N. G. High Efficiency Solid-State Sensitized Solar Cell-Based On Submicrometer Rutile

TiO$_2$ Nanorod and CH$_3$NH$_3$PbI$_3$ Perovskite Sensitizer. *Nano Lett.* **2013**, *13*, 2412–2417.

19. Fakharuddin, A.; Jose, R.; Brown, T. M.; Fabregat-Santiago, F.; Bisquert, J. A Perspective on the Production of Dye-Sensitized Solar Modules. *Energy Environ. Sci.* **2014**, *7*, 3952–3981.

20. Maçaira, J.; Andrade, L.; Mendes, A. Review on Nanostructured Photoelectrodes for Next Generation Dye-Sensitized Solar Cells. *Renewable Sustainable Energy Rev.* **2013**, *27*, 334–349.

21. Zhang, Q.; Cao, G. Nanostructured Photoelectrodes for Dye-Sensitized Solar Cells. *Nano Today* **2011**, *6*, 91–109.

22. Liu, B.; Aydil, E. S. Growth of Oriented Single-Crystalline Rutile TiO$_2$ Nanorods on Transparent Conducting Substrates for Dye-Sensitized Solar Cells. *J. Am. Chem. Soc.* **2009**, *131*, 3985–3990.

23. Snaith, H. J.; Abate, A.; Ball, J. M.; Eperon, G. E.; Leijtens, T.; Noel, N. K.; Stranks, S. D.; Wang, J. T. W.; Wojciechowski, K.; Zhang, W. Anomalous Hysteresis in Perovskite Solar Cells. *J. Phys. Chem. Lett.* **2014**, *5*, 1511–1515.

24. Shao, Y.; Xiao, Z.; Bi, C.; Yuan, Y.; Huang, J. Origin and Elimination of Photocurrent Hysteresis by Fullerene Passivation in CH$_3$NH$_3$PbI$_3$ Planar Heterojunction Solar Cells. *Nat. Commun.* **2014**, *5*, 5784.

25. Kim, H. S.; Park, N. G. Parameters Affecting I−V Hysteresis of CH$_3$NH$_3$PbI$_3$ Perovskite Solar Cells: Effects of Perovskite Crystal Size and Mesoporous TiO$_2$ Layer. *J. Phys. Chem. Lett.* **2014**, *5*, 2927–2934.

26. Even, J.; Pedesseau, L.; Katan, C. Analysis Of Multivalley and Multibandgap Absorption and Enhancement of Free Carriers Related to Exciton Screening in Hybrid Perovskites. *J. Phys. Chem. C* **2014**, *118*, 11566–11572.

27. Reese, M. O.; Gevorgyan, S. A.; Jørgensen, M.; Bundgaard, E.; Kurtz, S. R.; Ginley, D. S.; Olson, D. C.; Lloyd, M. T.; Morvillo, P.; Katz, E. A.; et al. Consensus Stability Testing Protocols for Organic Photovoltaic Materials and Devices. *Sol. Energy Mater. Sol. Cells* **2011**, *95*, 1253–1267.

28. Kim, J. H.; Williams, S. T.; Cho, N.; Chueh, C. C.; Jen, A. K. Y. Enhanced Environmental Stability of Planar Heterojunction Perovskite Solar Cells Based on Blade-Coating. *Adv. Energy Mater.* **2015**, 10.1002/aenm.201401229.

29. Niu, G. W.; Li, W.; Meng, F.; Wang, L.; Dong, H.; Qiu, Y. Study On The Stability Of CH$_3$NH$_3$PbI$_3$ Films and the Effect of Post-Modification By Aluminum Oxide in All-Solid-State Hybrid Solar Cells. *J. Mater. Chem. A* **2014**, *2*, 705–710.

30. Mei, A.; Li, X.; Liu, L.; Ku, Z.; Liu, T.; Rong, Y.; Xu, M.; Hu, M.; Chen, J.; Yang, Y.; Grätzel, M.; Han, H. A Hole-Conductor-Free, Fully Printable Mesoscopic Perovskite Solar Cell with High Stability. *Science* **2014**, *345*, 295–298.

31. Badia, L.; Mas-Marzá, E.; Sánchez, R. S.; Barea, E. M.; Bisquert, J.; Mora-Seró, I. New Iridium Complex as Additive to the Spiro-MeoTAD in Perovskite Solar Cells with Enhanced Stability. *APL Mater.* **2014**, *2*, 081507.

32. Habisreutinger, S. N.; Leijtens, T.; Eperon, G. E.; Stranks, S. D.; Nicholas, R. J.; Snaith, H. J. Carbon Nanotube/Polymer Composites as a Highly Stable Hole Collection Layer in Perovskite Solar Cells. *Nano Lett.* **2014**, *14*, 5561–5568.

33. Ahmed, I.; Fakharuddin, A.; Wali, Q.; Zainun, A. R. B.; Ismail, J.; Jose, R. Mesoporous Titania−Vertical Nanorod Films with Interfacial Engineering for High Performance Dye-Sensitized Solar Cells. *Nanotechnology* **2015**, *26*, 105401–105408.

34. Vesce, L.; Riccitelli, R.; Soscia, G.; Brown, T. M.; Di Carlo, A.; Reale, A. Optimization of Nanostructured Titania Photoanodes for Dye-Sensitized Solar Cells: Study and Experimentation of TiCl$_4$ Treatment. *J. Non-Cryst. Solids* **2010**, *356*, 1958–1961.